# SI-traceable validation of a laser spectrometer for balloon-borne measurements of water vapor in the upper atmosphere

Simone Brunamonti[1], Manuel Graf[1], Tobias Bühlmann[2], Céline Pascale[2], Ivan Ilak[1], Lukas Emmenegger[1] and Béla Tuzson[1]

[1]Empa – Swiss Federal Laboratories for Materials Science and Technology, Laboratory for Air Pollution/Environmental Technology, Dübendorf, Switzerland
[2]METAS – Swiss Federal Institute of Metrology, Laboratory Gas Analysis, Berne-Wabern, Switzerland

*Correspondence to:* Simone Brunamonti (simone.brunamonti@empa.ch) and Béla Tuzson (bela.tuzson@empa.ch)

**Abstract.** Despite its crucial role in the Earth's radiative balance, upper air water vapor ($H_2O$) is still lacking accurate, in-situ, and continuous monitoring. Especially in the upper troposphere-lower stratosphere (UTLS), these measurements are notoriously difficult, and significant discrepancies were reported in the past between different measuring techniques. Here, we present a laboratory assessment of a recently developed mid-IR quantum-cascade laser absorption spectrometer for balloon-borne measurements of $H_2O$ in the UTLS, alias ALBATROSS. The validation was performed using SI-traceable reference gas mixtures generated based on the permeation method and dynamic dilution. The accuracy and precision of ALBATROSS were evaluated at a wide range of pressures (30–250 mbar) and $H_2O$ amount fractions (2.5–35 ppm), representative of the atmospheric variability of $H_2O$ in the UTLS. Best agreement was achieved by implementing a quadratic Speed-Dependent Voigt Profile (qSDVP) line-shape model in the spectroscopic retrieval algorithm. The molecular parameters required by this parameterization were determined empirically using a multi-spectrum fitting approach over different pressure conditions. In the laboratory environment, ALBATROSS achieves an accuracy better than ±1.5 % with respect to the SI-traceable reference at all investigated pressures and $H_2O$ amount fractions. The measurement precision was found to be better than 30 ppb (i.e., 0.1 % at 35 ppm $H_2O$) at 1 s resolution for all conditions. This performance, unprecedented for a balloon-borne hygrometer, demonstrates the exceptional potential of mid-IR laser absorption spectroscopy as a new reference method for in-situ measurements of $H_2O$ in the UTLS.

## 1. Introduction

Water vapor ($H_2O$) is the strongest greenhouse gas in the Earth's atmosphere and a major driver of the atmospheric dynamics, microphysics, and interaction with radiation (IPCC, 2021). Its abundance in the atmosphere decreases strongly with altitude, from typically 1–3 % close to the surface, to around 5 µmol/mol (or parts per million, ppm) in the stratosphere. Despite its

scarcity, upper air $H_2O$ is still of great importance to the radiative balance of the atmosphere. Particularly, in the upper tropo-sphere-lower stratosphere (UTLS), i.e. at altitudes of about 8–25 km, even small changes in $H_2O$ were shown to have significant impact on the rate of global warming (Solomon et al., 2010; Riese et al., 2012). Hence, accurate measurements of $H_2O$ in the UTLS are crucial for reliable climate predictions. However, due to its low amount fraction and the low temperatures ($T <$ –60 °C) of the UTLS, accurate measurements of $H_2O$ in this region are notoriously difficult.

Since the pioneering work by Brewer and Dobson (1951), a large amount of scientific research has been done on the water vapor distribution and variability in the upper atmosphere, based on a wide range of platforms and analytical techniques (e.g., Scott et al., 1999; Rosenlof et al., 2001; Gurlit et al., 2005; Sargent et al., 2013; Buchholz et al., 2014; Meyer et al., 2015). Several studies comparing in-situ measurements of UTLS $H_2O$ from both aircraft and balloon platforms found significant discrepancies between different measuring techniques (e.g., Oltmans et al., 2000; Vömel et al., 2007; Rollins et al., 2014; Brunamonti et al., 2019; Singer et al., 2022), with implications for the understanding of ice microphysical processes (e.g., Peter et al., 2006; Krämer et al., 2009). Large relative discrepancies (exceeding ±100 %) between different hygrometers were also reported from laboratory experiments simulating the UTLS conditions, such as AquaVIT-1 (Fahey et al., 2014, and references therein), where only a small subset of instruments were able to achieve mean deviations below ±10 % from a reference value at all conditions.

Currently, cryogenic frost-point hygrometry (CFH/FPH) is considered as a state-of-the-art method for balloon-borne measurements of UTLS $H_2O$ (Fahey et al., 2014) and is routinely used in global long-term monitoring networks, such as the GCOS Reference Upper Air Network (GRUAN) (e.g., Hurst et al., 2011). CFH/FPH instruments are based on the chilled-mirror principle and have an estimated uncertainty of 4–6 % in the UTLS (Hall et al., 2016; Vömel et al. 2016). However, these devices are currently undergoing a fundamental reconception, because the cooling agent fluoroform (HFC-23) used for their operation must be phased out due its high global warming potential (UNEP, 2016). Thus, there is an urgent need for alternative, reliable technologies for the long-term monitoring of UTLS $H_2O$. Alternative measurement techniques demonstrated for light-weight balloon platforms include Lyman-α fluorescence (Zöger et al., 1999; Sitnikov et al., 2007; Khaykin et al., 2013) and laser absorption spectroscopy (Durry et al., 2008; Graf et al., 2021).

The aim of this work is to validate the accuracy and precision of a newly developed open-path, mid-IR quantum-cascade laser absorption spectrometer (Graf et al., 2021). This direct absorption-based technique has the promise of being a calibration-free method (Buchholz and Ebert, 2018), which makes it exceptionally attractive for demanding field applications. In practice, however, the accuracy can suffer from uncertainties in physical (pressure, temperature) as well as molecule-specific spectroscopic parameters, which will ultimately limit the quality of the retrieved data. While the error contribution of the environmental factors can be estimated based on the measurement uncertainties of these quantities, their large variations encountered in the stratosphere will also impact the intrinsic molecular properties of the absorption line, such as the line strength, its temperature dependence, and the pressure broadening parameters. Especially, a detailed knowledge of the latter is a prerequisite

for an accurate spectral retrieval. Our focus was on the broadening effects, while for the line strength and its temperature dependency we take the values from the HITRAN 2020 database (Gordon et al., 2022).

Here, we address this aspect by a dedicated laboratory investigation conducted at the Swiss Federal Institute of Metrology (METAS). Using a dynamic-gravimetric permeation method (e.g., Haerri et al., 2017; Guillevic et al., 2018), we generated SI-traceable $H_2O$ amount fractions as low as 2.5 ppm in synthetic air with an expanded measurement uncertainty smaller than ±1.5 %. This allowed us to improve our spectroscopic retrieval algorithm by implementing a more advanced line shape model than the standard Voigt profile, i.e., the quadratic Speed-Dependent Voigt Profile (qSDVP), and then to assess the accuracy and precision of ALBATROSS at a wide range of UTLS-relevant conditions. The molecular parameters required by the qSDVP parameterization were determined experimentally using a multi-spectrum fitting approach (e.g., Cygan and Lisak, 2017).

## 2. Experimental setup

### 2.1. ALBATROSS spectrometer

The ALBATROSS spectrometer, described in detail in Graf et al. (2021), leverages on recent advances in optics and laser driving concepts. It incorporates a monolithic, segmented circular multipass cell (SC-MPC), consisting of a rotationally symmetric arrangement of individual mirror segments carved into its inner surface (Graf et al., 2018). This geometry was found to be highly tolerant to thermally induced distortion, robust to mechanical stress, and thus, well suited for open-path applications (Tuzson et al., 2020). The SC-MPC contains 57 mirror segments (6×6 mm$^2$) with a diagonal distance of 108.8 mm, resulting in an effective optical path length (OPL) of 610.7 cm. The last segment of the SC-MPC is designed such that the laser beam is directly focused onto the IR-detector without any additional beam-shaping optics. A distributed feedback quantum cascade laser (DFB-QCL), packaged in a high-heat-load housing with embedded thermoelectric cooling and collimation optics (Alpes Lasers SA, Switzerland), is used as a light source. The laser is tuned across a ~1 cm$^{-1}$ spectral window centered around an isolated $H_2^{16}O$ absorption line at 1662.809 cm$^{-1}$ ($\lambda \approx 6.01$ μm). This absorption line corresponds to the transition 221←212 with a lower state energy of 79.5 cm$^{-1}$, which makes it largely insensitive to temperature. For example, a temperature change of 1 K would give < 0.13 % change in the observed absorption amplitude. Since we take this effect into account in our calculations, and because the ambient temperature is maintained constant, the impact of this term can safely be considered negligible. Furthermore, the estimated uncertainty of the line strength for the selected transition is known, according to the HITRAN database, with an accuracy better than 2 %.

A thermoelectrically-cooled MCT detector (PVM-2TE-8 1×1, Vigo Systems, Poland) is used for the detection of the transmitted light. Rapid spectral sweeping of the QCL is achieved by periodic modulation of the laser driving current, following the intermittent continuous wave (ICW) modulation approach (Fischer et al., 2014). In this approach, the laser driving current is applied in pulses (typically 100 μs long), followed by a short period of complete shutdown of the QCL. The ICW driving is obtained using custom-developed analogue electronics (Liu et al., 2018). The spectra are acquired at a frequency of 3 kHz and

co-averaged to a resolution of 1 Hz. A full description of the laser driving and data acquisition systems can be found in Graf et al. (2021). The spectrometer weights 3.41 kg, including batteries and a Styrofoam thermal insulation enclosure.

For its laboratory operation, ALBATROSS was set up into a closed-path configuration, in which the SC-MPC is closed on both sides by stainless-steel lids. The lids, as well as all tubes in contact with the gas, were treated by a highly inert coating (SilcoNert®2000, SilcoTek, USA) that minimizes the adsorption of molecules on its surface (e.g., Vaittinen et al., 2018; Macé et al., 2022), thereby minimizing memory effects and shortening the response time. The required leak-tightness was achieved by using nitrile O-rings (between the cell body and the lids), and high-vacuum metal fittings (VCR, Swagelok, USA) for the gas handling system. The SC-MPC volume in closed-path configuration is about 140 cm$^3$. Furthermore, the free-space path between the key optical elements, i.e. laser-MPC-detector (kept by design as short as physically possible, in our case, 2.7 cm) was enclosed by a custom-made flexible PEEK-tubing that is purged with dry $N_2$ and maintained slightly above atmospheric pressure, to avoid any "parasitic" $H_2O$ absorption from these external path sections.

## 2.2. Reference gas generation

The SI-traceable reference gas mixtures used for the validation of ALBATROSS were generated based on the permeation method combined with dynamic dilution (following ISO 6145-7 and ISO 6145-10). This is an established, standardized technique in metrology, particularly for reactive or polar compounds (e.g., Scaringelli et al., 1970; Brewer et al., 2011; Haerri et al., 2017; Guillevic et al., 2018). The setup used here is the same as described in Guillevic et al. (2018). All parts in contact with the gas mixture are passivated with SilcoNert®2000. The mass loss of the permeator is determined by a magnetic suspension balance (MSB, Rubotherm, Germany) under controlled temperature and pressure. This allows for continuous and unperturbed mass measurements, as the permeator is physically decoupled from the balance. To correct for balance drift and buoyancy, two calibration masses traceable to the SI realization of the kilogram of Switzerland (Fuchs et al., 2012) are automatically placed on the balance plate at regular intervals during the calibration routine. The permeator used here (Fine Metrology, Italy) has a nominal permeation rate of approximately 10 µg/min at 45 °C for $H_2O$ and was filled with ultrapure water (resistivity 18.2 MΩ cm at 25 °C, corresponding to a purity > 99.999 %). The expanded relative measurement uncertainty of the generated $H_2O$ amount fractions, determined upon calibration of the permeator including its drift and the dynamic dilution unit, was found to be better than ±1.5 % at all conditions.

As the isotopic composition of our water standard is not known, we estimate an additional uncertainty of about ±0.02 % on the total $H_2O$ amount fraction, by assuming that the liquid water standard has the signature of typical tap water, i.e., −60 ‰ $\delta^2H$ and −10 ‰ $\delta^{18}O$. Considering the low abundance of the heavy isotopologues and a natural distribution, the total $H_2O$ amount fraction contains about 99.73 % of the light water isotopologue ($H_2^{16}O$). Since ALBATROSS measures only this water isotopologue species and not the total $H_2O$ amount fraction, the reference values generated by the permeation method were scaled by this factor for the accuracy assessment.

## 2.3. Gas handling system

Figure 1 shows a schematics of the dilution and sampling system used for the measurements. The carrier gas is synthetic air that is passed through a gas purifier (MicroTorr MC400, Saes, Italy), which reduces the $H_2O$ content to about 70 ppb (previously measured by cavity-ring down spectroscopy). The volumetric flow rates in the different branches of the dilution and sampling system are controlled by a series of mass flow controllers (MFCs). The humidity content of the reference gas flow is adjusted by varying the flow rate of the dry synthetic air through MFC 2 between 0.05 slpm (corresponding to ~35 ppm $H_2O$) and 4.5 slpm (~2.5 ppm $H_2O$) to dilute the $H_2O$-enriched air stream that passes at a constant flow rate of 0.3 slpm (set by MFC 1) through the permeation chamber of the MSB. The total flow rate through the SC-MPC is kept constant at 0.3 slpm by MFC 3, while a solenoid valve allows the automatic switching between the reference gas mixture and the zero air (i.e., dry synthetic air) supplies. A vacuum pump and an upstream pressure controller (PC-15PSIA, Alicat, USA) are used to set the pressure in the multipass cell at various levels between 30–250 mbar. The sample pressure in the SC-MPC was monitored by a heated capacitance manometer (AA02, MKS Instruments, USA), with an absolute accuracy of 0.12 %. The standard deviation of the measured pressure was within 0.1 % during all experiments. All measurements were performed in an air conditioned laboratory and the spectrometer was operated inside a custom-made PMMA plastic chamber (thickness 15 mm) to further suppress any sudden temperature or humidity fluctuations. The temperature was monitored in the vicinity of the multipass cell (inside the PMMA chamber) by a HMP110 sensor (Vaisala, Finland), with an absolute accuracy of 0.2 °C. The average temperature measured during the campaign period was $23.5 \pm 0.03$ °C.

In addition to the SI-traceable reference gas mixtures, another series of measurements were performed using a secondary reference gas mixture. This allowed us to extend the range of the validation beyond the maximum value of 35 ppm $H_2O$. The custom-made secondary reference gas was produced by spiking a gas cylinder of synthetic air with a known amount of pure water. For this purpose, a regular steel cylinder (previously containing synthetic air) was evacuated, filled with synthetic air up to 1 bar, and then a syringe with distilled water was used to introduce a given amount of $H_2O$, followed by pressurizing the gas cylinder with synthetic air (with <5 ppm $H_2O$ content, Messer, Switzerland) up to 100 bar, resulting in a humidity content of about 180 ppm $H_2O$. After a few days of equilibration, the gas was expanded into a 34 L SilcoNert®2000-coated stainless-steel cylinder (Essex Industries Inc, USA) to further minimize any potential surface effects during the measurements.
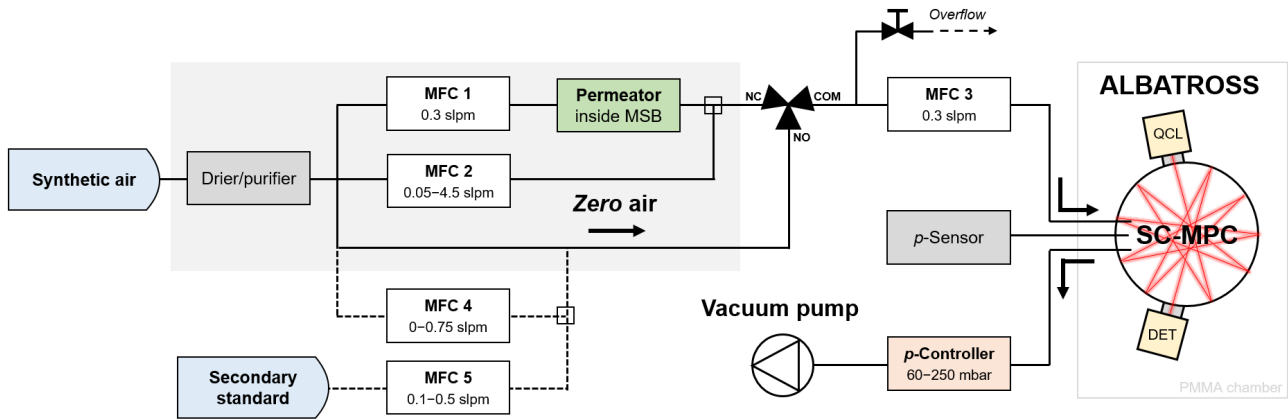
**Figure 1. Scheme of the sampling system used for the validation measurements. The grey shaded area indicates the magnetic suspension balance (MSB) and the dilution system used for the generation of the SI-traceable reference gases.**

5    It should be noted that this custom-made secondary reference gas does not fulfill SI-traceability, and it is subject to well-known long-term stability issues. Its sole purpose is to assess whether ALBATROSS is capable to measure significantly higher water vapor amounts than can be generated by the permeation method.

## 2.4. Measurements overview

The $H_2O$ amount fraction levels (or "setpoints") and gas pressure ($p$) levels were selected to be representative of the atmos-
10    pheric profile of $H_2O$ in the UTLS. Figure 2a shows the distribution of all $H_2O$ setpoints and $p$-levels investigated in this work, overlaid with two atmospheric profiles of $H_2O$ amount fraction measured by CFH during recent field campaigns. The profiles correspond to moist, tropical summer conditions (black line) and dry, mid-latitude winter conditions (grey line).
We selected five $H_2O$ setpoints covering the full range offered by the dynamic-gravimetric reference gas generation source (2.5–35 ppm), and eight $p$-levels between 30–250 mbar, for a total of 40 possible combinations (red crosses in Figure 2a). This
15    allows to fully cover the expected variability range of UTLS $H_2O$. The generated $H_2O$ amount fractions and selected $p$-levels, along with their relative uncertainties, are listed in Table 1. The conditions generated using the secondary reference gas mixtures for the extended-range validation (blue crosses in Figure 2a) included five $H_2O$ setpoints (between approximately 22–180 ppm) and three $p$-levels (60, 100, 200 mbar). These measurements allow to assess the linearity of ALBATROSS up to conditions relevant for the upper troposphere, i.e., roughly 6–10 km altitude.
20    Figure 2b shows a representative time series of the measurement performed at 150 mbar. Each $H_2O$ setpoint generated by the dynamic gravimetric method is measured for 2 h to allow the equilibration of the $H_2O$ amount fraction in the SC-MPC (Figure 2b). The last 30 min of each interval are then selected for the precision assessment. Before and after each experiment, the SC-

MPC is purged with zero air for at least 3 h to obtain the "empty-cell" spectrum, i.e. the transmission signal of the SC-MPC in the absence of the reference gas. This is used to normalize the subsequent raw absorption spectra. Despite the substantial purging by dry zero air, the lowest measured $H_2O$ amount fraction in the SC-MPC was about 1.5 ppm after 3 h of purging. This behavior is mainly due to the strong surface adsorption/desorption properties of $H_2O$, causing a memory effect to the system. Throughout the validation experiments, we observed a tendency towards slightly elevated zero levels whenever the gas pressure in the sampling line was lowered. Furthermore, the response time of the instrument showed a clear correlation with the humidity content of the measured gas.
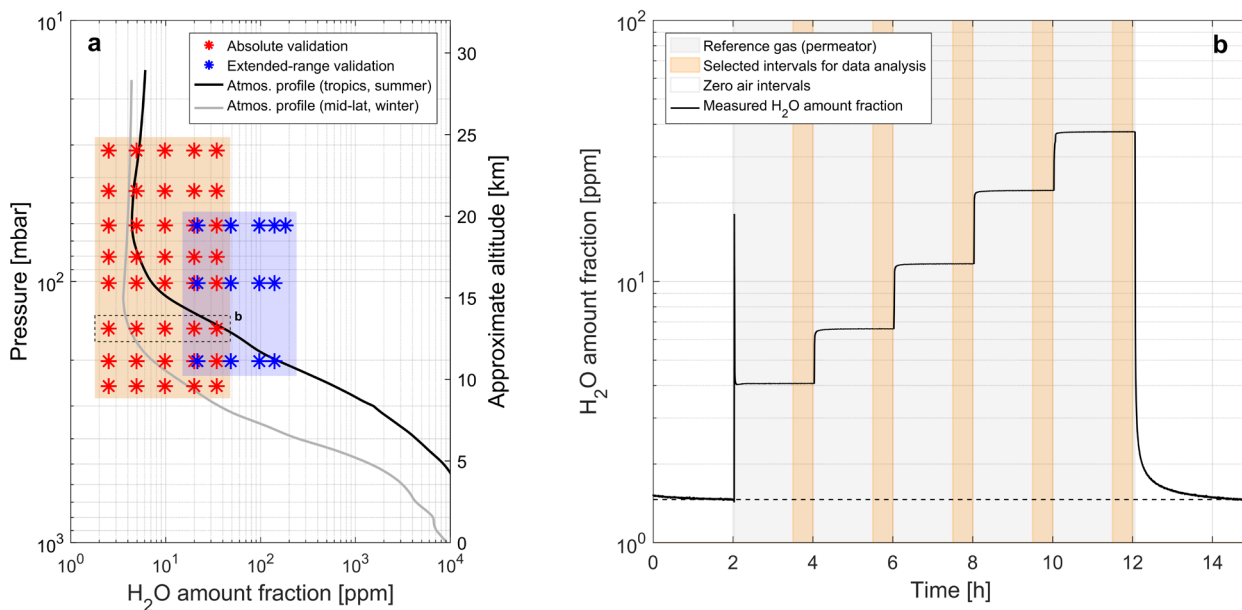
**Figure 2. Overview of the laboratory validation measurements. Panel (a): experimental settings in terms of pressure (*p*) and $H_2O$ amount fraction levels investigated for the absolute validation (red stars, SI-traceable reference) and the extended-range validation (blue stars, secondary reference) measurements, overlaid with two atmospheric profiles of UTLS $H_2O$. The profiles correspond to tropical summer conditions (black: Brunamonti et al., 2018) and mid-latitude winter conditions (grey: Graf et al., 2021) and were smoothed by a ±1 km moving average. Panel (b): time-series of the $H_2O$ amount fraction measured during the individual experiment at 150 mbar gas pressure, retrieved using the qSDVP line shape model at 1 s resolution. Different color shadings indicate zero air measurements (white), reference gas measurements (grey), and the 30 min intervals selected for the data analysis of each $H_2O$ level (orange). The estimated $H_2O$ amount fraction content of the zero air (1.46 ppm) is indicated by a black dashed line.**

While these effects may, if not properly taken into account, e.g. by the empty-cell spectrum normalization, affect the accuracy of the measurements, they are largely absent during flight conditions, where the instrument is operated in open-path configuration. In this latter case, there is no sampling line, the gas flow is much larger, and the surfaces of the SC-MPC are drastically reduced, as the lids are removed and the gas-surface interaction is limited to the narrow inner circumference of the cell.

**$H_2O$ amount fraction, Reference levels**

| Target value [ppm] | Actual value [ppm] |
|---|---|
| 2.5 | 2.514 ± 0.037 |
| 5 | 4.93 ± 0.07 |
| 10 | 9.84 ± 0.14 |
| 20 | 20.05 ± 0.28 |
| 35 | 34.58 ± 0.51 |

**Pressure levels**

| Target value [mbar] | Actual value [mbar] |
|---|---|
| 30 | 31.52 ± 0.04 |
| 45 | 45.14 ± 0.05 |
| 60 | 61.13 ± 0.07 |
| 80 | 80.67 ± 0.1 |
| 100 | 101.55 ± 0.12 |
| 150 | 151.75 ± 0.18 |
| 200 | 201.96 ± 0.24 |
| 250 | 251.62 ± 0.3 |

**Table 1. Summary of the $H_2O$ amount fraction levels generated by the dynamic-gravimetric method and their expanded measurement uncertainty (top) and pressure levels and their measurement uncertainty (bottom) used for the absolute validation. The relative expanded measurement uncertainty on the $H_2O$ amount fraction levels varies between 1.4−1.47 % for all conditions.**

## 3. Data analysis

### 3.1. Spectroscopic retrieval

The $H_2O$ amount fractions are retrieved from the measured spectra using the Beer-Lambert law in combination with the ideal gas law. Molecular line parameters are taken from the HITRAN2020 database (Gordon et al., 2022), and the wavenumber-dependency of the absorption coefficient is approximated by a line shape model. Typically, the Voigt profile (VP), a convolution of Gaussian (Doppler-broadening) and Lorentzian (pressure broadening) profiles, is considered as a good compromise to capture the pressure broadening effects while offering a good stability and reliability for airborne hygrometers (e.g., Buchholz et al., 2014; 2017; Graf et al. 2021). However, there is growing experimental evidence that various non-Voigt effects (e.g., Dicke narrowing, line narrowing due to speed dependence of pressure-induced broadening, and line asymmetry caused by speed dependence of pressure shift) can impact the observed absorption line profile (e.g., Hodges et al., 2008; Kochanov, 2012; Ngo et al., 2012; Tennyson et al., 2014; Lisak et al., 2015). Thus, one major aim of this work was to identify the line shape model that provides the best accuracy and reliability throughout the entire range of UTLS conditions.

Recently, the Hartmann–Tran profile (HTP) has been recommended as a new standard in spectroscopic databases (Tennyson et al., 2014). However, this model requires a large number of line-specific parameters, which are difficult to determine considering the correlations between them and the relatively moderate signal-to-noise ratio (SNR) of our measured spectra. Therefore, we investigated lower-order models that could still reproduce the measured spectra at high fidelity (i.e., to nearly the experimental noise level). Our analysis revealed the quadratic speed-dependent Voigt profile (qSDVP), in which the speed-dependence of the relaxation rates are considered as the sole source of line broadening, to be the most suitable.

The qSDVP model is characterized by the phenomenological rate parameters $\Gamma_2$ and $\Delta_2$ to describe the quadratic dependence on the active-molecule speed of the pressure-broadening width and shift, in addition to the collisional width and shift ($\Gamma_0$ and $\Delta_0$) averaged over all speeds (Tennyson et al., 2014). While the molecular parameters required by the VP line shape model can be readily obtained from the HITRAN2020 database, the corresponding qSDVP parameters for the $H_2O$ transition used here are not available in the literature. Hence, we had to determine these parameters experimentally. The parameter optimization procedure is discussed in detail in Sections 3.3-3.4.

Once the molecular parameters are defined, the $H_2O$ amount fractions are retrieved by minimizing the squared differences between the measured spectra and the line shape model (i.e., the fitting residuals), using a Levenberg-Marquardt least squares algorithm (Press et al., 2007). The overall measurement uncertainty on the amount fractions retrieved by this method, associated with the uncertainty on the measured environmental parameters that are used in the calculation, is estimated to be less than 0.2 %. This results from combining the absolute uncertainties on the measured $p$ (0.12 %) and $T$ (0.06 %), and their variability throughout the measurement periods (standard deviations 0.05 % and 0.01 %, respectively). The uncertainty on the measured OPL (< 1 mm) contributes by less than 0.01 %.

## 3.2. Pre-processing

Prior to the spectroscopic retrieval, the raw spectra are pre-processed. This includes a normalization step, which can be done either by dividing each raw spectrum by the corresponding empty-cell spectrum (i.e., the transmission through the multipass cell filled with zero air), or by reconstructing the laser intensity baseline using a polynomial function (Graf et al., 2021). Then, the time domain is converted to the frequency domain using the transmission spectrum of a 2-inch long Ge–etalon, and the data are interpolated to an equally-spaced wavenumber grid. For this, a free spectral range (FSR) value of $0.02429$ cm$^{-1}$ was determined by optimizing the retrieved peak position of two neighboring absorption lines of $N_2O$ (measured at 100 mbar) to their line positions given in HITRAN2020 (see Figure S1 in Supplementary material). The spectral range covered by the QCL is $0.88$ cm$^{-1}$. The number of data points per spectrum is reduced by a factor of 4, i.e. from $2.1{\times}10^4$ to $5{\times}10^3$, by using the moving average approach, resulting in a uniform spectral-point resolution of $1.67{\times}10^{-4}$ cm$^{-1}$.

Figure 3 shows an overview of the measured spectra, normalized using the empty-cell transmission approach at $H_2O$ amount fractions of 2.5 ppm, 10 ppm , 35 ppm, and 140 ppm. These spectra were obtained by co-averaging 50 s of data, corresponding to a total number of $1.5{\times}10^5$ individual spectra. This choice is justified by the Allan-Werle deviation analysis, discussed in Section 4.1. The SNR, defined as the ratio of the peak absorption signal to the standard deviation of the measured spectrum, calculated in a frequency interval that excludes the absorption line center, is about 50 at 2.5 ppm $H_2O$ (Figure 3a) and 2000 at 140 ppm $H_2O$ (Figure 3d).

As the empty-cell spectrum can only be used in a closed-path configuration, we also tested the polynomial-baseline normalization approach for the case of open-path configuration of ALBATROSS, which is suitable for the evaluation of flight data. Therefore, we apply both normalization methods, and we show in the Supplementary material that they provide the same results in terms of accuracy of the retrieved $H_2O$ amount fractions (Figure S2).
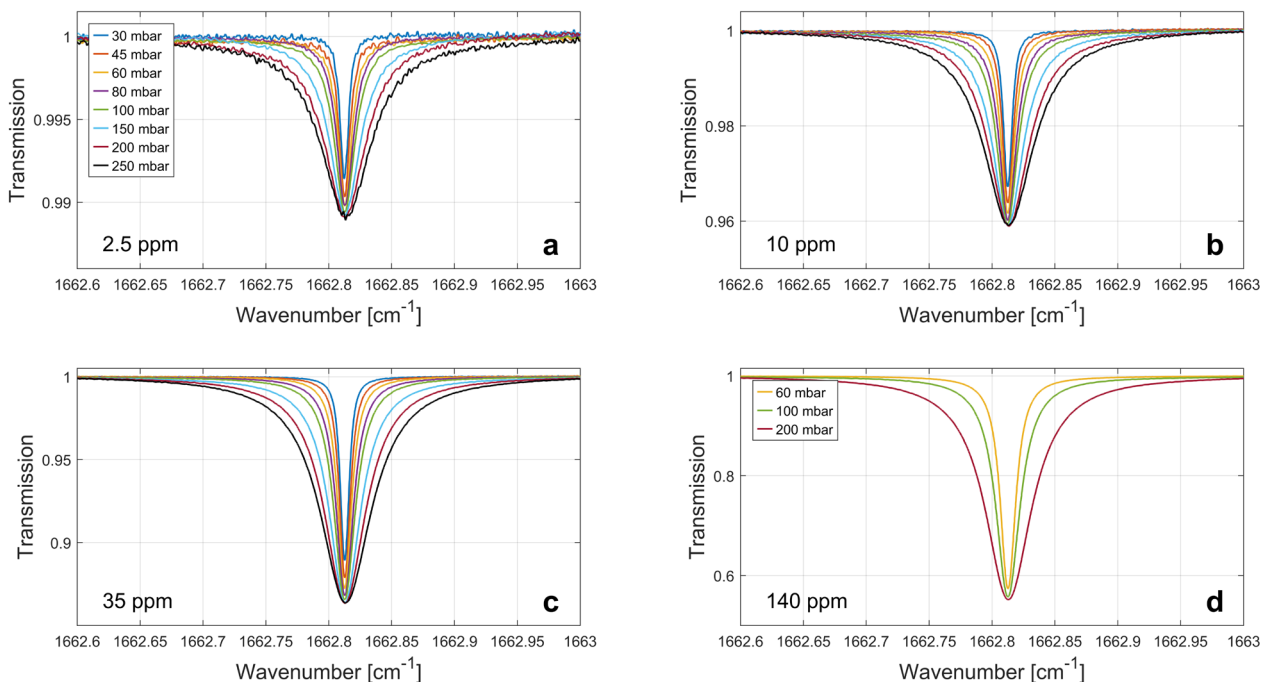
**Figure 3.** **Normalized transmission spectra measured during the laboratory validation experiments at 2.5 ppm (panel a), 10 ppm (b), 35 ppm (c), and 140 ppm $H_2O$ (d), color-coded with gas pressure. The SI-traceable reference gas mixtures (panels a-c) were measured at 8 pressure levels (30−250 mbar), while secondary reference gas mixtures (panel d) were measured at 3 pressure levels (60−200 mbar). All spectra shown here are integrated over 50 s.**

### 3.3. Voigt profile (VP)

As mentioned above, we first evaluated the performance of the VP model using the molecular parameters provided by the HITRAN2020 database, as well as by optimizing its parameters to obtain the best quality of the fit and agreement with the SI-traceable reference. However, neither approach was found to provide a sufficient level of accuracy or a good quality of the fit (QF). Here, the QF is defined, following Cygan et al. (2012), as the ratio of the peak absorption signal to the standard deviation of the fit residuals, calculated over the entire spectrum. This definition accounts not only for the random noise in the experimental spectrum, as in the case of SNR, but also for systematic distortions caused by limitations in the line shape model (Cygan et al., 2012).

The optimization of the line profile parameters was performed using a multi-spectrum fitting (MSF) approach, in which spectra recorded at different pressures are fitted simultaneously by the least-squares algorithm (e.g., Cygan and Lisak, 2017). This method has the advantage to eliminate the partial correlations between the different line-profile parameters that can occur in least-squares fits to single-pressure spectra. The procedure was implemented in Python using the HITRAN Application Programming Interface (HAPI) routines (Kochanov et al., 2016) as core engine for the spectral fitting.

The performance of the VP was evaluated based on the difference in $H_2O$ amount fraction between the spectroscopic retrievals and the SI-traceable reference values ($\Delta H_2O$), and the QF index. Figure 4 illustrates the VP optimization process, in terms of $\Delta H_2O$ (panel a) and QF index (b) calculated from fitting the spectra recorded at 35 ppm $H_2O$ and eight different pressures (as shown in Figure 3c), as function of the pressure broadening coefficient ($\Gamma_0$). This was obtained by using prescribed values of $\Gamma_0$ in the least-squares algorithm. Vertical dashed lines indicate the $\Gamma_0$ values from the HITRAN2020 database, namely 0.1002 $cm^{-1}$ $atm^{-1}$ at standard temperature (296 K) and pressure (1 atm) (STP conditions), and the value obtained by the MSF approach applied to the spectra measured at 35 ppm $H_2O$ and pressures 30−250 mbar ($\Gamma_0 = 0.0925$ $cm^{-1}$ $atm^{-1}$ at STP). All the line shape parameter values used for the retrieval are summarized in Table 2.

As a first step, the retrieval was performed using the $\Gamma_0$ and line strength ($S_{ij} = 8.63 \times 10^{-20}$ $cm^{-1}$/(molecule $cm^{-2}$) at 296 K) parameters specified in HITRAN2020. However, these settings result in an overestimation of the retrieved $H_2O$ amount fractions by up to 5 % compared to the reference value (Figure 4a), and a substantial spread of the deviations obtained at different pressures, indicating an increasing bias correlated with pressure (also shown in Figure 8 below). Therefore, we used the MSF algorithm to optimize the $\Gamma_0$ value over the 8 spectra considered here. This leads to the maximum of the QF index (Figure 4b), but in this case, the retrieved $H_2O$ amount fractions underestimate the reference value by up to 9 % (Figure 4a). Finally, we considered the case of varying $S_{ij}$, as recent studies reported slightly different values of this parameter compared to HITRAN2020 for the $H_2O$ transition considered here (Ptashnik et al., 2016; Conway et al., 2017; Birk et al., 2017; Delahaye et al., 2021). In this case, we observe that increasing the line strength parameter by 5 % compared to HITRAN2020 (consistent with Ptashnik et al., 2016), it is possible to obtain on average a good agreement with the reference values.
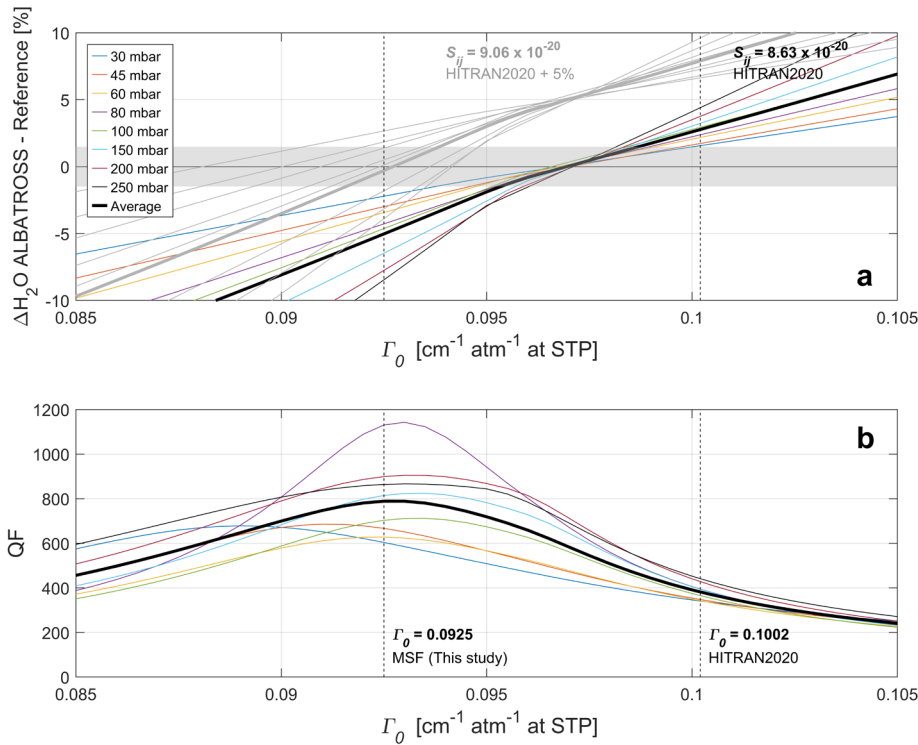
**Figure 4. Voigt profile (VP) optimization. Panel (a): difference in $H_2O$ amount fraction between the spectroscopic retrievals and the SI-traceable reference values ($\Delta H_2O$) at 35 ppm $H_2O$ and different pressures (color-coded), as function of the pressure broadening coefficient ($\Gamma_0$). The grey shaded area represents the relative uncertainty of the $H_2O$ reference levels generated by the permeator ($\pm 1.5\%$). Colored lines represent the results obtained using the line strength parameter ($S_{ij}$) from HITRAN2020, while grey lines using a 5 % higher $S_{ij}$ (given in units of $cm^{-1}$/(molecule $\cdot$ $cm^{-2}$) at 296 K). Panel (b): quality of the fit (QF) index as function of $\Gamma_0$, obtained from the VP model. Vertical dashed lines indicate the $\Gamma_0$ values obtained from the HITRAN2020 database (0.1002 $cm^{-1}$ $atm^{-1}$ at STP) and by the MSF approach (0.0925 $cm^{-1}$ $atm^{-1}$ at STP). In both panels, a thick black line shows the average value over all pressure levels.**

The major drawback of this approach is that the calibration-free character of the retrieval is lost, because the optimization of the line strength value relies on the assumption of a target $H_2O$ concentration value. Furthermore, the good agreement found for one particular pressure does not apply for each individual pressure level, and a pressure-related bias still affects the results (see spread of grey lines in Figure 4a at $\Gamma_0 = 0.0925$ $cm^{-1}$ $atm^{-1}$ at STP). Hence, we conclude that the VP model is unable to reproduce the observed spectral characteristics with sufficiently high accuracy.

### 3.4. Quadratic speed-dependent Voigt profile (qSDVP)

After showing the limitations of the VP model, we proceeded to improve our spectroscopic retrieval algorithm to the qSDVP parameterization. To determine the required parameters, the MSF algorithm was applied to the spectra collected at 140 ppm $H_2O$ and pressure levels 60−200 mbar (shown in Figure 3d). This $H_2O$ level was chosen to achieve the highest possible SNR (i.e., about 2000), which is critical for an accurate estimation of the higher-order line shape parameters. To avoid overfitting, we fixed the $\Delta_0$ and $S_{ij}$ parameters to their values given in HITRAN2020 and set $\Delta_2 = 0$ (the reason for this is given below), while the most critical $\Gamma_0$ and $\Gamma_2$ parameters were determined by the MSF algorithm. As will be shown below, this configuration is highly efficient to fully reproduce the measured spectra at high fidelity, and with high accuracy of the retrieved $H_2O$ amount fractions. The parameters resulting from the MSF calculation are namely $\Gamma_0 = 0.0992$ cm$^{-1}$ atm$^{-1}$ and $\Gamma_2 = 0.0135$ cm$^{-1}$ atm$^{-1}$ at STP.

To illustrate that this approach provides a robust estimate of the pressure broadening parameters, Figure 5 shows a contour map of the QF index as function of $\Gamma_0$ and $\Gamma_2$. This was obtained by consecutively varying $\Gamma_0$ and $\Gamma_2$ stepwise within a 25×25 grid, centered around their value obtained from the MSF method. The QF index shown here is calculated as the average QF over the three pressure levels measured at 140 ppm $H_2O$ (60, 100, and 200 mbar).

**Line shape model parameters**

| | Voigt profile (VP) | | qSDVP |
|---|---|---|---|
| *Parameter* | HITRAN2020 | *This study* | *This study* |
| $S_{ij}$ [cm$^{-1}$/molec cm$^{-2}$] | $8.63 \times 10^{-20}$ | $8.63 \times 10^{-20\,(*)}$ | $8.63 \times 10^{-20}$ |
| $\Delta_0$ [cm$^{-1}$ atm$^{-1}$] | $3.87 \times 10^{-3}$ | $3.87 \times 10^{-3}$ | $3.87 \times 10^{-3}$ |
| $\Gamma_0$ [cm$^{-1}$ atm$^{-1}$] | 0.1002 | 0.0925 | 0.0992 |
| $\Delta_2$ [cm$^{-1}$ atm$^{-1}$] | *N.A.* | *N.A.* | 0 |
| $\Gamma_2$ [cm$^{-1}$ atm$^{-1}$] | *N.A.* | *N.A.* | 0.0135 |

**Table 2. Summary of molecular parameters used for the spectroscopic retrieval. For the Voigt profile (VP) model, both the values taken from the HITRAN2020 database and those determined in this study are reported. The quadratic Speed-Dependent Voigt Profile (qSDVP) parameters were determined in this study, as discussed in Section 3. All values are expressed for standard temperature and pressure (STP) conditions (i.e., 296 K, 1 atm). (*) Note that a 5 % higher $S_{ij}$ value was also tested for the VP optimization (Figure 4), and slightly different estimates of $S_{ij}$ for this transition are also reported in the literature (see Section 3.3). The $\Gamma_2$ and $\Delta_2$ parameters are not applicable (N.A.) to the VP parameterization.**

The results show that our MSF estimate of $\Gamma_0$ and $\Gamma_2$ lies in a well-defined maximum of the QF index (i.e., minimum of the standard deviation of the residuals), with values slightly exceeding 2000 (Figure 5). This QF matches the SNR of the measured

spectra, which is a strong indication that the line-shape model reproduces the measured spectra to the experimental noise level. It is important to realize that in this case, the line profile parameters are solely determined by the QF. The MSF algorithm is not aware of the target (or "true") value of the $H_2O$ concentration, it simply tries to minimize the sum of the squares of the residuals, i.e. the difference between the observed value and the fitted value provided by the model. Here, the model is based on first principles using the molecular parameters and the physical quantities ($p$, $T$, OPL). The generated SI-traceable $H_2O$ concentrations are only used comparison purposes only. There is no calibration involved.

Finally, Figure 6 shows the fit residuals obtained using the VP (panels a-b) and qSDVP (c-d) line shape models, at 35 ppm $H_2O$ (panels a, c) and 140 ppm $H_2O$ (b, d). The VP retrieval is performed using the line parameters from the HITRAN2020 database, while for the qSDVP we use the $\Gamma_0$ and $\Gamma_2$ coefficients determined by the MSF method. Using VP yields systematic residuals significantly exceeding the measurement noise and exhibiting the characteristic W-shape, with deviations as large as 1 % of the absorption signal near the line center (Figure 6b). Conversely, using qSDVP, the fit residuals stay below ~0.1 % of the transmission signal for all pressures and $H_2O$ amount fractions (Figure 6c-d). It can be tempting to include additional line profile parameter, e.g. $\Delta_2$ to further reduce the remaining structures. However, our primary aim is to find an optimum compromise between establishing a reliable and accurate spectral retrieval, while maintaining the high temporal (spatial) resolution of the spectrometer during balloon flights. The latter requires that we evaluate spectra from the flights at 1 s acquisition time rather than averaging them over, e.g., 50 s. However, as the noise scales by $\sqrt{t}$ (assuming random fluctuations), its amplitude is about 7 times larger in the 1 s data compared to the situation shown in the Figure 6, and thus, random noise-induced statistical effects dominate the spectra. In our opinion, including another degree of freedom for the spectral fit under such circumstances is largely questionable. Another aspect is the consideration of various artifacts and their impact on the measured line profiles. As indicated by the Figure S1, the FSR determination uncertainty in our case is about $1.3 \times 10^{-5}$ cm$^{-1}$. Furthermore, the frequency stability of our free running QCL at longer time scales was found to be between 1.2 and $5.5 \times 10^{-5}$ cm$^{-1}$ (mainly determined by the laser heat-sink temperature stability). While the former term affects the frequency scale accuracy, the latter has a random bias on the line profile when averaging over multiple acquisitions. These influences can easily induce slight asymmetries or subtle line-shape distortions that can be than erroneously assigned to the $\Delta_2$ parameter. Moreover, our trial of using $\Delta_2$ as a free fitting parameter in the MSF routine, resulted in a weakly constrained value with large uncertainties, indicating difficulties of a proper assignment. Similarly, we also found that considering other parameters, e.g. collisional narrowing, does
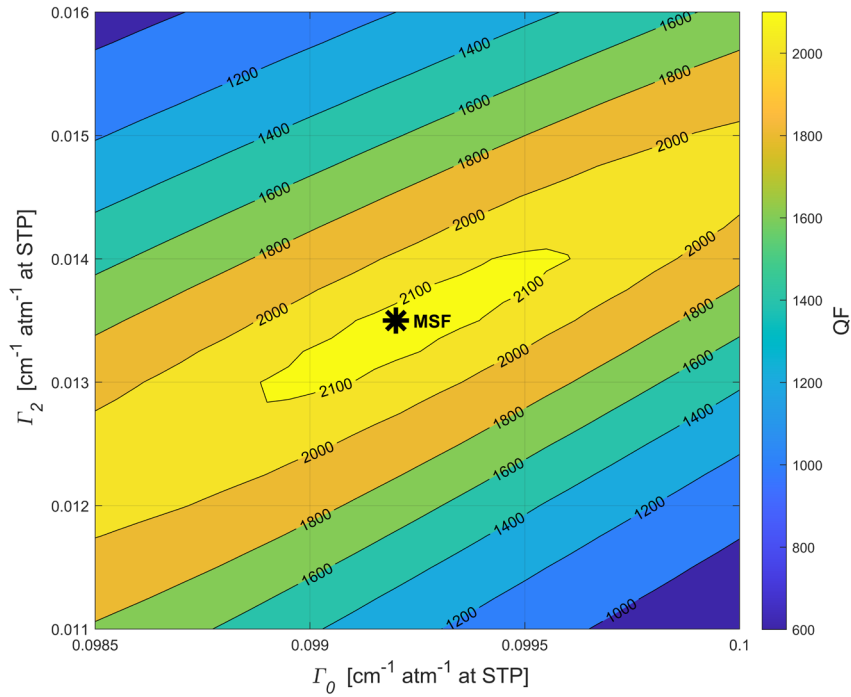
**Figure 5. Determination of the qSDVP fitting parameters. Contour map of quality of the fit (QF) index as function of $\Gamma_0$ and $\Gamma_2$, obtained by fitting a qSDVP profile to the spectra recorded at 140 ppm H$_2$O. The $\Gamma_0$ and $\Gamma_2$ values obtained from the MSF approach applied to the same spectra ($\Gamma_0$ = 0.0992 cm$^{-1}$ atm$^{-1}$, $\Gamma_2$ = 0.0135 cm$^{-1}$ atm$^{-1}$ at STP) are indicated by a star. The QF index is calculated**
5  **as the average QF over the three pressure levels measured at 140 ppm H$_2$O (60, 100, and 200 mbar). The map was obtained by varying $\Gamma_0$ and $\Gamma_2$ in a regular 25×25 grid with a resolution of 6×10$^{-5}$ cm$^{-1}$ atm$^{-1}$ in $\Gamma_0$ and 2×10$^{-4}$ cm$^{-1}$ atm$^{-1}$ in $\Gamma_2$.**

not improve the QF index. Therefore, we conclude, in full agreement with previous works (e.g., Lisak et al.., 2015), that the observed line shapes can be well reproduced by assigning the non-Voigt effects to speed-dependent effects rather than colli-
10  sional narrowing. These facts justify the choice of a reduced model against a generalized higher-order (HTP) parameterization.
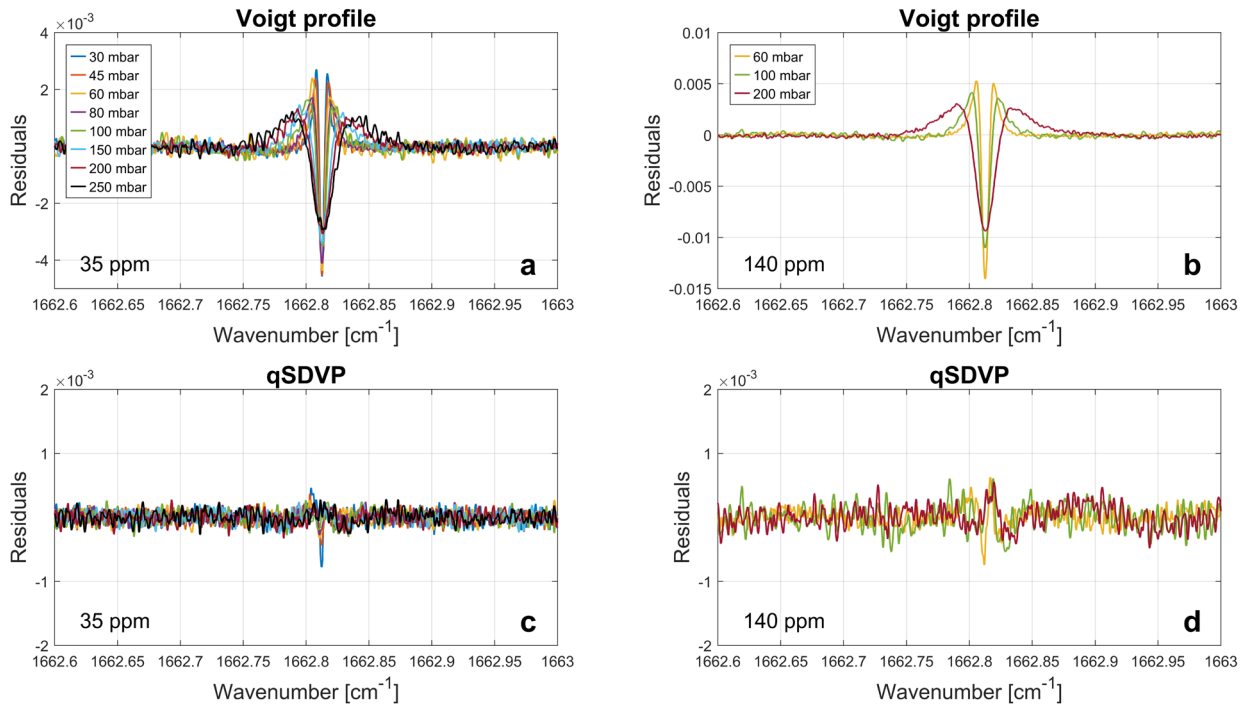
**Figure 6.** Fit residuals obtained using a Voigt profile (VP, panels a-b) and quadratic Speed-Dependent Voigt Profile (qSDVP, panels c-d) line shape model at 35 ppm $H_2O$ (panels a, c) and 140 ppm $H_2O$ (b, d), color-coded with pressure. The VP fit is performed using molecular parameters from the HITRAN2020 database, while the qSDVP fitting uses the $\Gamma_0$ and $\Gamma_2$ values determined from the MSF approach.

## 4. Results

### 4.1. Precision and long-term stability

The precision and long-term stability of ALBATROSS are assessed using 30 min of data recorded at 1 s resolution, taken at the end of each measurement interval (see Figure 2b). In particular, the Allan-Werle deviation technique (Allan, 1966; Werle et al., 1993) was used to determine the measurement precision as a function of integration time, and to distinguish between instrumental drifts and random noise (Werle et al., 1993). The analysis was repeated using both the VP and qSDVP retrievals, revealing no impact on the measurement precision by the choice of line shape model. The results shown in the following were obtained with the qSDVP model and the parameters determined as discussed above.

Figure 7 shows frequency of occurrence histograms (left) and Allan-Werle deviation plots (right) for a selection of $H_2O$ amount fractions and pressure levels. The frequency of occurrence distributions, color-coded with pressure, correspond to 2.5, 10, and

35 ppm $H_2O$ (panels a-c). Each distribution is calculated in 40 bins of 5 ppb width, centered around the mean $H_2O$ amount fraction. Allan-Werle deviation as function of integration time are shown for all pressures at 2.5 ppm $H_2O$ (panel d), and for all $H_2O$ setpoints at 150 mbar (e). The theoretical line corresponding to white-noise behavior ($\sim \tau^{-1/2}$ where $\tau$ = integration time) is also indicated on panels d-e as a reference.
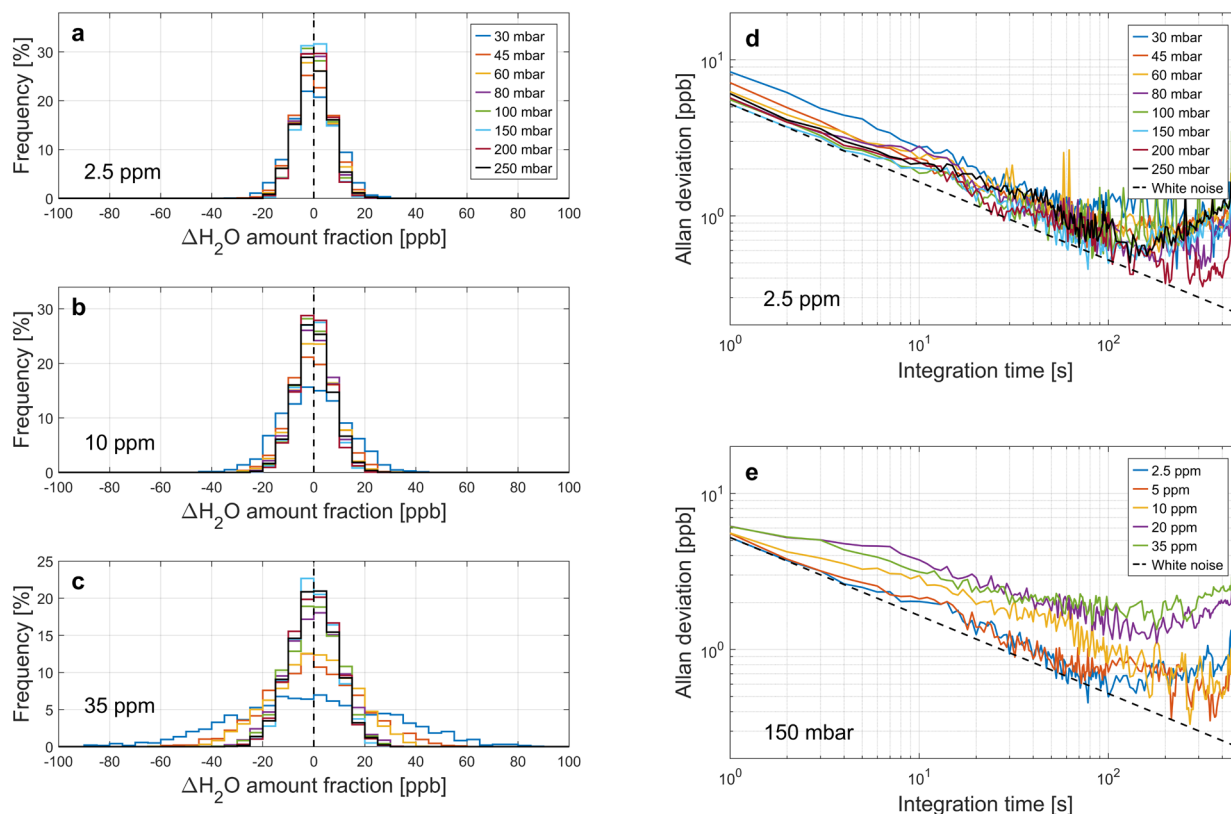
**Figure 7. Precision and long-term stability assessment. Panels (a-c): frequency of occurrence distributions calculated over 30 min of measurements at 1 s resolution for 2.5 ppm $H_2O$ (a), 10 ppm (b), and 35 ppm (c), color-coded with pressure. Each distribution is calculated using 40 bins of 5 ppb width, centered on the mean $H_2O$ amount fraction measured at the corresponding setpoint and pressure. Panels (d-e): Allan-Werle deviation plots for all pressures at 2.5 ppm $H_2O$ (panel d), and for all $H_2O$ setpoints at pressure level 150 mbar (e). The white-noise behavior ($\sim \tau^{-1/2}$, where $\tau$ = integration time) is indicated on panels (d-e) as a reference.**

The frequency of occurrence distributions are generally very narrow (within ±30 ppb) at all conditions (Figure 7a-b), with a few exceptions at low pressures and high water amount fractions (Figure 7c). The standard deviation ($\sigma_{1\,s}$) of the distributions

shown in Figure 7a-c vary between 6–9 ppb (corresponding to 0.23–0.33 % of the reference value) at 2.5 ppm $H_2O$, 7–13 ppb (0.07–0.13 %) at 10 ppm $H_2O$, and 9–30 ppb (0.03–0.08 %) at 35 ppm $H_2O$. On average over all pressures, $\sigma_{1s}$ lies between 0.04 % (14 ppb) at 35 ppm $H_2O$, and 0.25 % (7 ppb) at 2.5 ppm $H_2O$.

The Allan-Werle deviation plots indicate a stable operation of the spectrometer up to 100 s, after which drifts start to dominate the measurements. This can be due to mechanical and optical instabilities of the instrument, but also due to flow rate fluctuations of the MFCs. The Allan deviation minimum is always reached at integration times between 50–100 s, corresponding to a precision between 0.5–5 ppb (i.e., 0.02–0.5 % of the reference value). Therefore, an integration time of 50 s was selected for the accuracy assessment and for the determination of the qSDVP parameters. Investigating the time-series of the zero air measurements over longer time scales indicated that the spectrometer maintains a stable operation over a few hours, at least. The Allan-Werle deviation minimum in this case stayed at a constant value of 0.5 ppb $H_2O$ after about 2 min averaging (see Figure S3 in Supplementary material).

## 4.2. Accuracy

The accuracy of ALBATROSS is evaluated by comparing the spectroscopically retrieved $H_2O$ amount fractions with the SI-traceable reference $H_2O$ values generated by the dynamic-gravimetric method (as listed in Table 1), at each pressure level. To quantify the improvement in accuracy obtained by the qSDVP parameterization, the results are also compared to those obtained using the VP line shape model and HITRAN2020 molecular parameters.

Figure 8 shows the relative difference in $H_2O$ amount fraction between the ALBATROSS retrievals (integrated over 50 s) and the reference values ($\Delta H_2O$), as function of pressure and color-coded with the $H_2O$ setpoint. The error bars correspond to 1 $\sigma$ standard deviation. The relative uncertainty on the $H_2O$ reference levels generated by the permeator ($\pm1.5$ %) is indicated by the grey shaded area.

The results show that all measurements retrieved using the qSDVP line shape model are found within the $\pm1.5$ % uncertainty range of the permeator, hence in excellent agreement with the SI-traceable reference values. In contrast, the VP retrievals (with $\Gamma_0$ and $S_{ij}$ from HITRAN2020) systematically overestimate the amount fractions by 1.5–5 % compared to the reference, with a bias increasing with pressure.

Using qSDVP, the largest relative deviation from the reference occurs at 2.5 ppm $H_2O$ and 45 mbar (+1.05%, corresponding to +27 ppb $H_2O$), while the largest absolute deviation is found at 35 ppm $H_2O$ and 100 mbar (+0.79 %, i.e., +273 ppb $H_2O$). On average over all pressures, $\Delta H_2O$ varies between +0.01 % (i.e., +0.1 ppb) at 10 ppm $H_2O$, and +0.22 % (+5.5 ppb) at 35 ppm $H_2O$. The pressure-averaged $\Delta H_2O$ values and their corresponding standard deviations are summarized in Table 3. This excellent agreement reflects the high quality of the molecular parameters listed in the HITRAN database and their well confined uncertainties, at least for the $H_2O$ transition selected for our study.
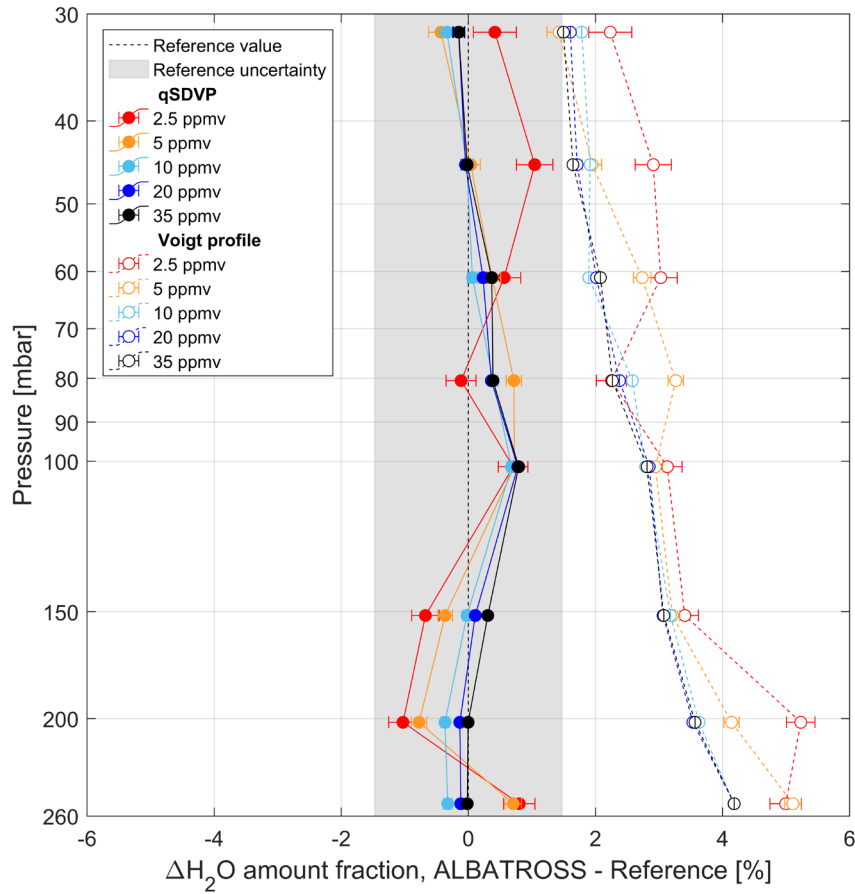
**Figure 8. Accuracy assessment. Relative difference in H₂O amount fraction between the spectroscopic retrievals and the reference values (ΔH₂O) as function of pressure, color-coded with H₂O amount fractions. Results obtained using the qSDVP line shape model are shown as filled circles and solid lines, while Voigt profile (VP) results are shown as open circles and dashed lines. The error bars on each data point correspond to the 1 $\sigma$ standard deviation. The expanded relative uncertainty of the H₂O reference levels generated by the dynamic-gravimetric method (±1.5 %) is indicated by the grey shaded area.**

**Accuracy and precision**

| Setpoint [ppm] | Absolute deviation [ppb] | Relative deviation [%] |
|:---:|:---:|:---:|
| 2.5 | + 5.5 ± 7 | + 0.22 ± 0.25 |
| 5 | + 6.1 ± 7 | + 0.12 ± 0.14 |
| 10 | + 0.1 ± 8 | + 0.01 ± 0.08 |
| 20 | + 26 ± 11 | + 0.13 ± 0.05 |
| 35 | + 72 ± 14 | + 0.21 ± 0.04 |

**Table 3. Accuracy and precision of the ALBATROSS measurements performed during the validation. Absolute and relative deviations are expressed as ΔH₂O ±1 $\sigma$, where ΔH₂O is the H₂O amount fraction difference between the ALBATROSS retrievals and the SI-traceable reference levels and $\sigma$ the standard deviation, both averaged over all the considered pressure levels (30–250 mbar).**

5    Furthermore, it also demonstrates that beyond-Voigt line-profile models have the capability to accurately describe the observed shape of the absorption line, opening the path to a highly accurate quantification of the observed data.

## 4.3. Linearity (extended-range validation)

The aim of the extended-range validation was to characterize the linearity of ALBATROSS beyond the upper limit of 35 ppm $H_2O$ delivered by the dynamic-gravimetric method. For this, the custom-made secondary reference gas (not SI-traceable),

10   prepared as described in Section 2.3, was diluted to four different $H_2O$ amount fraction levels using two mass flow controllers (MFCs 4-5 in Figure 1). The linearity of the spectrometer is assessed by comparing the spectroscopically retrieved $H_2O$ amount fractions with the calculated amount fractions based on the dilution ratio and the $H_2O$ content of the undiluted reference gas. The MFCs (Axetris, Switzerland) were calibrated at METAS using an SI-traceable primary standard with an accuracy of 0.2 % on volumetric flow rate. The dilution ratios are defined as the ratio of the flow rate of the secondary reference gas to the

15   total flow rate (kept constant) of secondary reference and dilution gas. The $H_2O$ amount fraction of the undiluted secondary reference gas, namely 183.54 ± 0.06 ppm, was determined by ALBATROSS at 60 mbar using the qSDVP line shape model and integration time 50 s. The calculated $H_2O$ amount fractions and their corresponding uncertainties obtained for each dilution step are listed in Table 4.

Figure 9 shows a scatter plot of the $H_2O$ amount fractions retrieved by ALBATROSS (using qSDVP and integrated over 50 s)

20   at 60 mbar versus the expected $H_2O$ amount fractions (panel a), and their difference (ΔH₂O) at 60, 100, and 200 mbar (panel b). The results of a linear fit (slope, intercept, and determination coefficient $R^2$) between the measured and the expected $H_2O$ amount fractions at 60 mbar are also displayed in panel a. As the $H_2O$ content of the undiluted cylinder was only determined

once, we estimate its uncertainty based on the repeatability of the measurement performed at 140 ppm (i.e., 310 ppb $H_2O$) and the precision of the single measurement at 180 ppm (60 ppb $H_2O$). This results in a total uncertainty of ± 370 ppb $H_2O$, i.e., roughly ± 0.2 % (as shown by the error bars in Figure 9b).

All spectroscopically retrieved $H_2O$ amount fractions are found in very good agreement with the expected values (within ±0.6 %), and with an excellent correlation over the entire investigated range (Figure 9). On average over all pressures, $\Delta H_2O$ varies between −0.22 ppm (i.e., −0.16 %) at 140 ppm $H_2O$, and +0.15 ppm (+0.31 %) at 48 ppm $H_2O$. The largest relative deviation was found at 22 ppm $H_2O$ and 200 mbar (−0.92 %, i.e., −0.20 ppm). The 1 $\sigma$ standard deviation varies between 13 ppb (0.06 %) at 22 ppm $H_2O$, and 30 ppb (0.02 %) at 140 ppm $H_2O$ (see Table 4).

Along with the results obtained with the SI-traceable reference gases in the range of 2.5–35 ppm $H_2O$, the extended-range validation demonstrates the outstanding performances of ALBATROSS at conditions that fully cover the expected variability of $H_2O$ in the UTLS (see Figure 2a). Although, these assessments were performed under well controlled laboratory environment using a closed-path configuration, we expect that the performance of the instrument will remain the same also during flight conditions. The demonstration of this behavior is beyond the scope of this study, however, some related aspects (the effects of turbulence, thermo-mechanical deformation, etc.) were described in our earlier studies (e.g., Tuzson et al. (2020), Graf (2020), Graf et al. (2021)). We found that the highly reduced optical complexity of ALBATROSS exhibits an excellent robustness against environmental impacts and its performance was not deteriorated.

**Linearity (extended-range validation)**

| Dilution ratio | Calculated H₂O amount fraction [ppm] | Measured H₂O amount fraction [ppm] | Absolute deviation [ppm] | Relative deviation [%] |
|---|---|---|---|---|
| 0.1187 ± 0.0004 | 21.78 ± 0.07 | 21.69 ± 0.01 | − 0.08 | − 0.38 |
| 0.2637 ± 0.0008 | 48.41 ± 0.15 | 48.56 ± 0.02 | + 0.15 | + 0.31 |
| 0.5261 ± 0.001 | 96.56 ± 0.18 | 96.45 ± 0.02 | − 0.11 | − 0.10 |
| 0.7650 ± 0.0007 | 140.41 ± 0.13 | 140.19 ± 0.03 | − 0.22 | − 0.16 |
| 1 | - | 183.54 ± 0.06 | - | - |

**Table 4. Summary of the extended-range validation measurements. Dilution ratios and calculated H₂O amount fractions are expressed as expected values ± the uncertainty associated with the volumetric flow rates measurements by the mass-flow controllers. Measured H₂O amount fractions are expressed as mean values ± 1 $\sigma$ the standard deviation, averaged over the three pressure levels considered here (60, 100 and 200 mbar). Absolute and relative deviations are the difference between measured and calculated H₂O amount fractions. Note that the undiluted H₂O amount fraction of the secondary reference gas (i.e., dilution ratio = 1) was measured by ALBATROSS at 60 mbar and is used to calculate the expected H₂O amount fractions at all levels.**
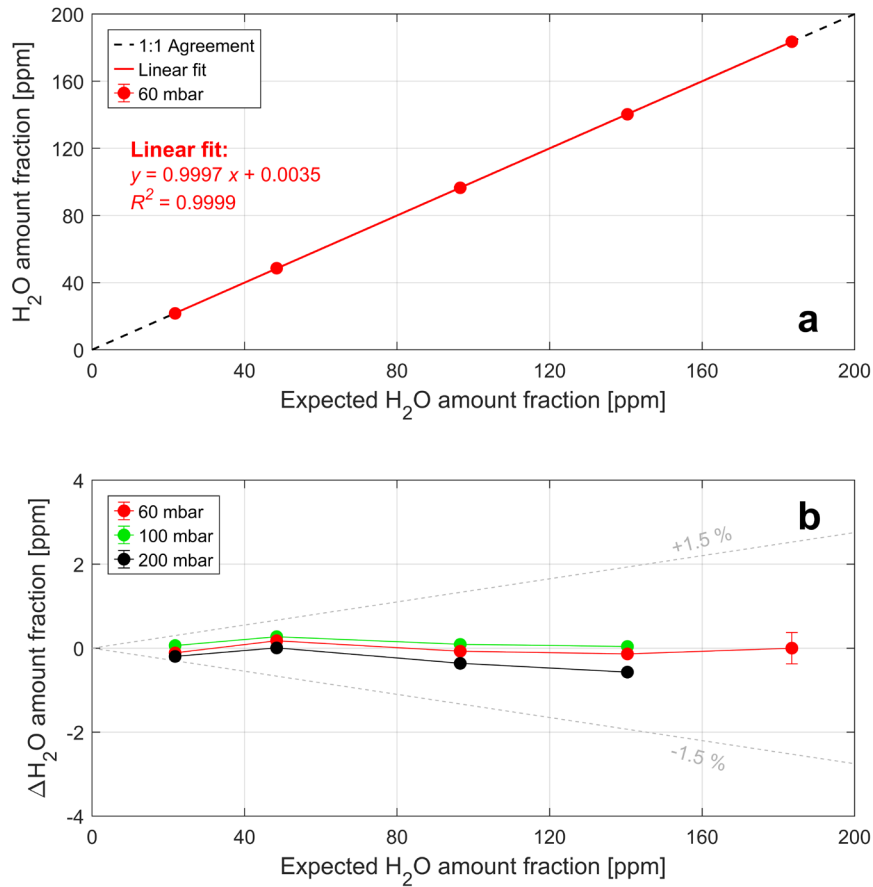
**Figure 9. Linearity assessment over the extended-range. Correlation plot of the $H_2O$ amount fractions retrieved by ALBATROSS (*y*-axis) versus the expected $H_2O$ amount fractions based on dilution ratio (*x*-axis) at 60 mbar (panel a), and their difference ($\Delta H_2O$) as function of the expected amount fractions at 60, 100, and 200 mbar (panel b). The grey dashed lines in panel (b) indicate a relative deviation of $\Delta H_2O = \pm 1.5$ %.**

This performance in terms of accuracy and precision makes ALBATROSS a particularly attractive tool for investigating the upper troposphere region. This can be of interest for cirrus clouds microphysical modeling (e.g., Luo et al., 2003; Reinares Martínes et al., 2020) and in-cloud supersaturation studies (e.g., Krämer et al., 2009; Dekoutsidis et al., 2023), requiring accurate $H_2O$ measurements at high vertical/temporal resolution as input parameters.

# 5. Conclusions

We have presented a detailed laboratory assessment of ALBATROSS, a newly developed quantum-cascade laser absorption spectrometer for balloon-borne measurements of $H_2O$ in the upper troposphere-lower stratosphere (UTLS). The validation was performed using SI-traceable reference gases generated by a dynamic-gravimetric permeation method, capable to deliver $H_2O$ amount fractions as low as 2.5 ppm in synthetic air, with an uncertainty smaller than ±1.5 %. The accuracy and precision of ALBATROSS were evaluated in a wide range of pressure (30–250 mbar) and $H_2O$ amount fractions (2.5–35 ppm), representative of the atmospheric variability of $H_2O$ in the UTLS. In addition, the linearity of ALBATROSS was verified up to 180 ppm $H_2O$ using a custom-made secondary reference gas mixture.

We found that the quadratic-speed-dependent Voigt profile (qSDVP) gives a quality of the fit that is commensurate with our spectral signal-to-noise ratio, and accurately reproduces the measured line shapes without any systematic bias over the entire pressure range. The molecular parameters required by this parameterization ($\Gamma_0$ and $\Gamma_2$) for the $H_2O$ line investigated here were determined experimentally using a multi-spectrum fitting (MSF) approach over multiple pressure conditions. Furthermore, we demonstrated that the implementation of the qSDVP line shape model, using these empirically determined broadening parameters (given in Table 2) improves the accuracy by up to 5 % compared to the VP model.

The measurements show that ALBATROSS achieves an accuracy better than ± 1.5 % with respect to the SI-traceable reference at all investigated pressures and $H_2O$ amount fractions. The measurement precision at 1 s resolution was found to be better than 30 ppb (i.e., 0.1 % at 35 ppm $H_2O$) at all conditions, and as low as 5 ppb (0.02 % at 35 ppm $H_2O$) upon integrating the data over 50 s, corresponding to the Allan deviation minimum. These results are particularly remarkable considering the technical challenges of maintaining a stable $H_2O$ amount fraction level in the low-ppm range in a laboratory setting, due to the strong surface adsorption/desorption properties of $H_2O$. Furthermore, the comparison between the normalization methods, i.e., empty-cell and polynomial-baseline (shown in the Supplementary material), demonstrates the applicability of these results to the analysis of real atmospheric (i.e., open-path) data as well.

The performance achieved by ALBATROSS is unprecedented for a light-weight balloon-borne hygrometer, and thus demonstrate the exceptional potential of mid-IR laser absorption spectroscopy as an alternative reference method to cryogenic frost-point hygrometry (CFH) for in-situ measurements of $H_2O$ in the UTLS. This is particularly relevant considering the ongoing phasing out of the cooling agent required by CFH (fluoroform, HFC-23), which urges the need of an alternative solution to maintain the monitoring of UTLS $H_2O$ in global, long-term monitoring networks, such as the GCOS Reference Upper Air Network (GRUAN).

Currently, ALBATROSS is participating in the AquaVIT-4 International Intercomparison of Atmospheric Hygrometers, held at the AIDA cloud simulation chamber (Karlsruhe Insitute of Technology, Germany). This will allow to characterize the performance of the spectrometer under a new set of challenging UTLS-relevant conditions, also in terms of temperature, and to

validate its accuracy against a set of well-established hygrometers (both laboratory-based and airborne). Finally, new inter-comparison test flights between CFH and ALBATROSS are foreseen to further validate the performances achieved in the laboratory in a real atmospheric environment.

**Data availability.** The data are available from the authors upon request.

**Competing interests.** The authors declare that they have no conflict of interest.

**Author contributions.** SB, MG and TB performed the measurements, under the supervision of BT and CP. SB performed the data analysis with the support from MG, II and BT. BT and LE supervised the project. SB and BT wrote the manuscript with contributions from all authors.

**Acknowledgements.** The ALBATROSS ("Balloon-borne laser spectrometer for UTLS water research") project was funded by the Federal Office of Meteorology and Climatology (MeteoSwiss), in the framework of GCOS (Global Climate Observing System) Switzerland. The authors thank Martin Vollmer (Empa) for support in the generation of the secondary reference gas mixture. Philipp Scheidegger, André Kupferschmid, and Herbert Looser are acknowledged for their continuous HW and SW support. We are grateful to Alan Fried, Markus Miltner, Daniele Romanini, and one anonymous reviewer for their constructive comments and valuable suggestions which helped us to improve this manuscript.

## References

Allan, D. W.: Statistics of Atomic Frequency Standards. Proc. IEEE, 54, 2, 221–230, ISSN 15582256, DOI:10.1109/PROC.1966.4634, 1966.

Birk, M., Wagner, G., Loos, J., Lodi, L., Polyansky, O. L., Kyuberis, A. A., Zobov, N. F., and Tennyson, J.: Accurate line intensities for water transitions in the infrared: Comparison of theory and experiment, J. Quant. Spectrosc. Radiat. Transf., 203, 88-102, https://doi.org/10.1016/j.jqsrt.2017.03.040, 2017.

Brewer, A. W., and Dobson, R. H.: An automatic frost-point hygrometer for measurements in the upper air. Proceedings of the Institute of Electrical and Eelectronics Engineers, 98(64), 470–473, 1951.

Brewer, P. J., Goody, B. A., Woods, P. T., and Milton, M. J. T.: A dynamic gravimetric standard for trace water, Rev. Sci. Instrum., 82, 105102, https://doi.org/10.1063/1.3642660, 2011.

Brunamonti, S., Jorge, T., Oelsner, P., Hanumanthu, S., Singh, B. B., Kumar, K. R., Sonbawne, S., Meier, S., Singh, D., Wienhold, F. G., Luo, B. P., Boettcher, M., Poltera, Y., Jauhiainen, H., Kayastha, R., Karmacharya, J., Dirksen, R., Naja, M., Rex, M., Fadnavis, S., and Peter, T.: Balloon-borne measurements of temperature, water vapor, ozone and aerosol backscatter on the southern slopes of the Himalayas during StratoClim 2016–2017, Atmos. Chem. Phys., 18, 15937–15957, https://doi.org/10.5194/acp-18-15937-2018, 2018.

Brunamonti, S., Füzér, L., Jorge, T., Poltera, Y., Oelsner, P., Meier, S., Dirksen, R., Naja, M., Fadnavis, S., Karmacharya, J., Wienhold, F. G., Luo, B. P., Wernli, H., and Peter, T.: Water Vapor in the Asian Summer Monsoon Anticyclone: Comparison of Balloon-Borne Measurements and ECMWF Data, J. Geophys. Res.-Atmos., 124, https://doi.org/10.1029/2018JD030000, 2019.

Buchholz, B., Afchine, A., and Ebert, V.: Rapid, optical measurement of the atmospheric pressure on a fast research aircraft using open-path TDLAS, Atmos. Meas. Tech., 7, 3653–3666, https://doi.org/10.5194/amt-7-3653-2014, 2014.

Buchholz, B., Afchine, A., Klein, A., Schiller, C., Krämer, M., and Ebert, V.: HAI, a new airborne, absolute, twin dual-channel, multi-phase TDLAS-hygrometer: background, design, setup, and first flight data, Atmos. Meas. Tech., 10, 35–57, https://doi.org/10.5194/amt-10-35-2017, 2017.

Buchholz, B. and Ebert, V.: Absolute, pressure-dependent validation of a calibration-free, airborne laser hygrometer transfer standard (SEALDH-II) from 5 to 1200 ppmv using a metrological humidity generator, Atmos. Meas. Tech., 11, 459–471, https://doi.org/10.5194/amt-11-459-2018, 2018.

Conway, E. K., Gordon, I. E., Kyuberis, A. A., Polyansky, O. L., Tennyson, J., and Zobov, N. F.: Calculated line lists for H216O and H218O with extensive comparisons to theoretical and experimental sources including the HITRAN2016 database, J. Quant. Spectrosc. Radiat. Transf., 241, 106711, https://doi.org/10.1016/j.jqsrt.2019.106711, 2020.

Cygan, A., Lisak, D., Wójtewicz, S., Domysławska, J., Hodges, J. T., Trawiński, R. S., and Ciuryło, R.: High-signal-to-noise-ratio laser technique for accurate measurements of spectral line parameters, Phys. Rev. A, Vol. 85, 022508, DOI: 10.1103/PhysRevA.85.022508, 2012.

Cygan, A., and Lisak, D.: Multi-spectrum fitting software for advanced spectral line shapes analysis, J. Phys.: Conf. Ser., 810 012025, doi:10.1088/1742-6596/810/1/012025, 2017.

Delahaye, T., Armante, R., Scott, N. A., Jacquinet-Husson, N., Chédin, A., Crépeau, L., Crevoisier, C., Douet, V., Perrin, A., Barbe, A., Boudon, V., Campargue, A., Coudert, L. H., Ebert, V., Flaud, J.-M., Gamache, R. R., Jacquemart, D., Jolly, A., Kwabia Tchana, F., Kyuberis, A., Li, G., Lyulin, O. M., Manceron, L., Mikhailenko, S., Moazzen-Ahmadi, N., Müller, H. S. P., Naumenko, O. V., Nikitin, A., Perevalov, V. I., Richard, C., Starikova, E., Tashkun, S. A., Tyuterev, Vl. G., Vander, Auwera, J., Vispoel, B., Yachmenev, A., and Yurchenko, S.: The 2020 edition of the GEISA spectroscopic database, J. Quant. Spectrosc. Radiat. Transf., 380, 111510, https://doi.org/10.1016/j.jms.2021.111510, 2021.

Dekoutsidis, G., Groß, S., Wirth, M., Krämer, M., and Rolf, C.: Characteristics of supersaturation in midlatitude cirrus clouds and their adjacent cloud-free air, Atmos. Chem. Phys., 23, 3103–3117, https://doi.org/10.5194/acp-23-3103-2023, 2023.

Durry, G., Amarouche, N., Joly, L., Liu, X., Parvitte, B., and Zéninari, V.: Laser diode spectroscopy of $H_2O$ at 2.63 µm for atmospheric applications, Appl. Phys. B, 90, 573–580, DOI: 10.1007/s00340-007-2884-3, 2008.

Fahey, D. W., Gao, R.-S., Möhler, O., Saathoff, H., Schiller, C., Ebert, V., Krämer, M., Peter, T., Amarouche, N., Avallone, L. M., Bauer, R., Bozóki, Z., Christensen, L. E., Davis, S. M., Durry, G., Dyroff, C., Herman, R. L., Hunsmann, S., Khaykin, S. M., Mackrodt, P., Meyer, J., Smith, J. B., Spelten, N., Troy, R. F., Vömel, H., Wagner, S., and Wienhold, F. G.: The AquaVIT-1 intercomparison of atmospheric water vapor measurement techniques, Atmos. Meas. Tech., 7, 3177–3213, https://doi.org/10.5194/amt-7-3177-2014, 2014.

Fischer, M., Tuzson, B., Hugi, A., Brönnimann, R., Kunz, A., Blaser, S., Rochat, M., Landry, O., Müller, A., and Emmenegger, L.: Intermittent operation of QC-lasers for mid-IR spectroscopy with low heat dissipation: tuning characteristics and driving electronics, Opt. Express, 22, 7014–7027, https://doi.org/10.1364/OE.22.007014, 2014.

Fuchs, P., Marti, K., and Russi, S.: New instrument for the study of "the kg, mise en pratique": first results on the correlation between the change in mass and surface chemical state, Metrologia, 49, 607–614, https://doi.org/10.1088/0026-1394/49/6/607, 2012.

Gordon, I.E., Rothman, L.S., Hargreaves, R.J., Hashemi, R., Karlovets, E.V., Skinner, F.M., Conway, E.K., Hill, C., Kochanov, R.V., Tan, Y., Wcisło, P., Finenko, A.A., Nelson, K., Bernath, P.F., Birk, M., Boudon, V., Campargue, A., Chance, K.V., Coustenis, A., Drouin, B.J., Flaud, J.–M., Gamache, R.R., Hodges, J.T., Jacquemart, D., Mlawer, E.J., Nikitin, A.V., Perevalov, V.I., Rotger, M., Tennyson, J., Toon, G.C., Tran, H., Tyuterev, V.G., Adkins, E.M., Baker, A., Barbe, A., Canè, E., Császár, A.G., Dudaryonok, A., Egorov, O., Fleisher, A.J., Fleurbaey, H., Foltynowicz, A., Furtenbacher, T., Harrison, J.J., Hartmann, J.–M., Horneman, V.–M., Huang, X., Karman, T., Karns, J., Kassi, S., Kleiner, I., Kofman, V., Kwabia–Tchana, F., Lavrentieva, N.N., Lee, T.J., Long, D.A., Lukashevskaya, A.A., Lyulin, O.M., Makhnev, V.Yu., Matt, W., Massie, S.T., Melosso, M., Mikhailenko, S.N., Mondelain, D., Müller, H.S.P., Naumenko, O.V., Perrin, A., Polyansky, O.L., Raddaoui, E., Raston, P.L., Reed, Z.D., Rey, M., Richard, C., Tóbiás, R., Sadiek, I., Schwenke, D.W., Starikova, E., Sung, K., Tamassia, F., Tashkun, S.A., Vander Auwera, J., Vasilenko, I.A., Vigasin, A.A., Villanueva, G.L., Vispoel, B., Wagner, G., Yachmenev A., and Yurchenko, S.N.: The HITRAN2020 molecular spectroscopic database, J. Quant. Spectrosc. Radiat. Transf., 277, 107949, https://doi.org/10.1016/j.jqsrt.2021.107949, 2022.

Graf, M., Emmenegger, L., and Tuzson, B.: Compact, circular, and optically stable multipass cell for mobile laser absorption spectroscopy, Opt. Lett., 43, 2434–2437, https://doi.org/10.1364/OL.43.002434, 2018.

Graf, M.: Balloon-borne Atmospheric Water Vapor Measurement by Laser Absorption Spectroscopy, Diss. ETH No. 26662 Submitted to ETH Zürich, Switzerland, https://doi.org/10.3929/ethz-b-000429788, 2020.

Graf, M., Scheidegger, P., Kupferschmid, A., Looser, H., Peter, T., Dirksen, R., Emmenegger, L., and Tuzson, B.: Compact and lightweight mid-infrared laser spectrometer for balloon-borne water vapor measurements in the UTLS, Atmos. Meas. Tech., 14, 1365–1378, https://doi.org/10.5194/amt-14-1365-2021, 2021.

Guillevic, M., Vollmer, M. K., Wyss, S. A., Leuenberger, D., Ackermann, A., Pascale, C., Niederhauser, B., and Reimann, S.: Dynamic–gravimetric preparation of metrologically traceable primary calibration standards for halogenated greenhouse gases, Atmos. Meas. Tech., 11, 3351–3372, https://doi.org/10.5194/amt-11-3351-2018, 2018.

Gurlit, W., Zimmermann, R., Giesemann, C., Fernholz, T., Ebert, V., Wolfrum, J., Platt, U., and Burrows, J. P.: Lightweight diode laser spectrometer CHILD (Compact High-altitude In-situ Laser Diode) for balloonborne measurements of water vapor and methane, Applied Optics, 44, 1, 91-102, https://doi.org/10.1364/AO.44.000091, 2005.

Haerri, H.-P., Macé, T., Waldén, J., Pascale, C., Niederhauser, B., Wirtz, K., Stovcik, V., Sutour, C., Couette, J., and Waldén, T.: Dilution and permeation standards for the generation of NO, $NO_2$ and $SO_2$ calibration gas mixtures, Meas. Sci. Technol., 28, 035801, https://doi.org/10.1088/1361-6501/aa543d, 2017.

Hall, E. G., Jordan, A. F., Hurst, D. F., Oltmans, S. J., Vömel, H., Kühnreich, B., and Ebert, V.: Advancements, measurement uncertainties, and recent comparisons of the NOAA frost point hygrometer, Atmos. Meas. Tech., 9, 4295–4310, https://doi.org/10.5194/amt-9-4295-2016, 2016.

Hodges, J. T., Lisak, D., Lavrentieva, N., Bykov A., Sinitsa, L., Tennyson, J., Barber, R. J., and Tolchenov, R. N.: Comparison between theoretical calculations and high-resolution measurements of pressure broadening for near-infrared water spectra, ournal of Molecular Spectroscopy, 249, 86–94, doi:10.1016/j.jms.2008.02.022, 2008.

Hurst, D. F., Oltmans, S. J., Vömel, H., Rosenlof, K. H., Davis, S. M., Ray, E. A., Hall, E. G., and Jordan, A. F.: Stratospheric water vapor trends over Boulder, Colorado: Analysis of the 30 year Boulder record. J. Geophys. Res.-Atmos., 116, D02306. https://doi.org/10.1029/2010JD015065, 2011.

IPCC: Climate Change 2021: The Physical Science Basis. Contribution of Working Group I to the Sixth Assessment Report of the Intergovernmental Panel on Climate Change [Masson-Delmotte, V., P. Zhai, A. Pirani, S.L. Connors, C. Péan, S. Berger, N. Caud, Y. Chen, L. Goldfarb, M.I. Gomis, M. Huang, K. Leitzell, E. Lonnoy, J.B.R. Matthews, T.K. Maycock, T. Waterfield, O. Yelekçi, R. Yu, and B. Zhou (eds.)]. Cambridge University Press, Cambridge, United Kingdom and New York, NY, USA, 2391 pp., doi:10.1017/9781009157896, 2021

Khaykin, S. M., Engel, I., Vömel, H., Formanyuk, I. M., Kivi, R., Korshunov, L. I., Krämer, M., Lykov, A. D., Meier, S., Naebert, T., Pitts, M. C., Santee, M. L., Spelten, N., Wienhold, F. G., Yushkov, V. A., and Peter, T.: Arctic stratospheric dehydration – Part 1: Unprecedented observation of vertical redistribution of water, Atmos. Chem. Phys., 13, 11 503–11 517, https://doi.org/10.5194/acp-13-450 11503-2013, 2013.

Kochanov, V. P.: On systematic errors in spectral line parameters retrieved with the Voigt line profile, J. Quant. Spectrosc. Radiat. Transf., 113, 1635–1641, http://dx.doi.org/10.1016/j.jqsrt.2012.03.024, 2012.

Kochanov, R. V., Gordon, I.E., Rothman, L.S., Wcislo, P., Hill, C., and Wilzewski, J.S.: HITRAN Application Programming Interface (HAPI): A comprehensive approach to working with spectroscopic data, J. Quant. Spectrosc. Radiat. Transf., 177, 15-30, https://doi.org/10.1016/j.jqsrt.2016.03.005, 2016.

Krämer, M., Schiller, C., Afchine, A., Bauer, R., Gensch, I., Mangold, A., Schlicht, S., Spelten, N., Sitnikov, N. M., Borrmann, S., de Reus, M., and Spichtinger, P.: Ice supersaturations and cirrus cloud crystal numbers, Atmos. Chem. Phys., 9, 3505–3522, 455 https://doi.org/10.5194/acp-9-3505-2009, 2009.

5    Lisak, D., Cygan, A., Bermejo, D., Domenech, J. L., Hodges, J. T., and Tran, H.: Application of the Hartmann–Tran profile to analysis of $H_2O$ spectra, J. Quant. Spectrosc. Radiat. Transf., 164, 221–230, http://dx.doi.org/10.1016/j.jqsrt.2015.06.012, 2015.

Liu, C., Tuzson, B., Scheidegger, P., Looser, H., Bereiter, B., Graf, M., Hundt, M., Aseev, O., Maas, D., and Emmenegger, L.: Laser driving and data processing concept for mobile trace gas sensing: Design and implementation, Rev. Sci. Instrum., 89, https://doi.org/10.1063/1.5026546, 2018.

10   Luo, B. P., Peter T., Fueglistaler, S., Wernli, H., Wirth, M., Kiemle, C., Flentje, H., Yushkov, V. A., Khattatov, V., Rudakov, V., Thomas, A., Borrmann, S., Toci, G., Mazzinghi, P., Beuermann, J., Schiller, C., Cairo, F., Di Donfrancesco, G., Adriani, A., Volk, C. M., Strom, J., Noone, K., Mitev, V., MacKenzie, R. A., Carslaw, K. S., Trautmann, T., Santacesaria, V., and Stefanutti, L.: Dehydration potential of ultrathin clouds at the tropical tropopause, Geophys. Res. Lett., 30, 1557, doi:10.1029/2002GL016737, 2003.

15   Macé, T., Iturrate-Garcia, M., Pascale, C., Niederhauser, B., Vaslin-Reimann, S., and Sutour, C.: Air pollution monitoring: development of ammonia (NH3) dynamic reference gas mixtures at nanomoles per mole levels to improve the lack of traceability of measurements, Atmos. Meas. Tech., 15, 2703–2718, https://doi.org/10.5194/amt-15-2703-2022, 2022.

Meyer, J., Rolf, C., Schiller, C., Rohs, S., Spelten, N., Afchine, A., Zöger, M., Sitnikov, N., Thornberry, T. D., Rollins, A. W., Bozóki, Z., Tátrai, D., Ebert, V., Kühnreich, B., Mackrodt, P., Möhler, O., Saathoff, H., Rosenlof, K. H., and Krämer, M.:
20   Two decades of water vapor measurements with the FISH fluorescence hygrometer: a review, Atmos. Chem. Phys., 15, 8521–8538, https://doi.org/10.5194/acp-15-8521-2015, 2015.

Ngo, N. H., Ibrahim, N., Landsheere, X., Tran, H., Chelin, P., Schwell, M., and Hartmann, J.-M.: Intensities and shapes of $H_2O$ lines in the near-infrared by tunable diode laser spectroscopy, J. Quant. Spectrosc. Radiat. Transf., doi:10.1016/j.jqsrt.2011.12.007, 2012.

25   Oltmans, S., Rosenlof, K., Michelsen, H., Nedoluha, G., Pan, L., Read, W., Remsberg, E., and Schiller, C.: SPARC Report No. 2: Upper Tropospheric and Stratospheric Water Vapour, Chapter 2, Tech. rep., https://www.sparc-climate.org/publications/sparc-reports/sparc-report-no-2/, 2000.

Peter, T., Marcolli, C., Spichtinger, P., Corti, T., Baker, M. B., and Koop, T.: When Dry Air Is Too Humid, Science, 314, 1399–1402, https://doi.org/10.1126/science.1135199, 2006.

30   Press, W. H., Teukolsky, S. A., Vetterling, W. T., and Flannery, B. P.: Numerical Recipes 3rd Edition: The Art of Scientific Computing, Cambridge University Press, New York, NY, USA, 2007.

Ptashnik, I. V., McPheat, R., Polyansky, O. L., Shine, K. P., and Smith, K. M.: Intensities and self-broadening coefficients of the strongest water vapour lines in the 2.7 and 6.25μm absorption bands, J. Quant. Spectrosc. Radiat. Transf., 177, 92-107, https://doi.org/10.1016/j.jqsrt.2016.02.001, 2016.

Reinares Martínez, I., Evan, S., Wienhold, F. G., Brioude, J., Jensen, E. J., Thornberry, T. D., Héron, D., Verreyken, B., Körner, S., Vömel, H., Metzger, J.-M., and Posny, F: Unprecedented observations of a nascent in situ cirrus in the tropical tropopause layer. Geophysical Research Letters, 48, e2020GL090936. https://doi.org/10.1029/2020GL090936, 2020.

Riese, M., Ploeger, F., Rap, A., Vogel, B., Konopka, P., Dameris, M., and Forster, P.: Impacts of uncertainties in atmospheric mixing on simulated UTLS composition and related radiative effects, J. Geophys. Res.-Atmos., 117, D16305. https://doi.org/10.1029/2012JD017751, 2012.

Rollins, A. W., Thornberry, T., Gao, R. S., Smith, J. B., Sayres, D. S., Sargent, M. R., Schiller, C., Krämer, M., Spelten, N., Hurst, D. F., Jordan, A. F., Hall, E. G., Vömel, H., Diskin, G. S., Podolske, J. R., Christensen, L. E., Rosenlof, K. H., Jensen, E. J., and Fahey, D. W.: Evaluation of UT/LS hygrometer accuracy by intercomparison during the NASA MAC-PEX mission, J. Geophys. Res.-Atmos., 119, 1915–1935, https://doi.org/10.1002/2013JD020817, 2014.

Sargent, M. R., Sayres, D. S., Smith, J. B., Witinski, M., Allen, N. T., Demusz, J. N., Rivero, M., Tuozzolo, C., and Anderson, J. G.: A new direct absorption tunable diode laser spectrometer for high precision measurement of water vapor in the upper troposphere and lower stratosphere, Rev. Sci. Instrum., 84, 074102, https://doi.org/10.1063/1.4815828, 2013.

Scaringelli, F. P., O'Keeffe, A. E., Rosenberg, E., and Bell, J. P.: Preparation of known concentrations of gases and vapors with permeation devices calibrated gravimetrically, Anal. Chem., 42, 871–876, https://doi.org/10.1021/ac60290a012, 1970.

Scott, D. C., Herman, R. L., Webster, C. R., May, R. D., Flesch, G. J., and Moyer, E. J.: Airborne Laser Infrared Absorption Spectrometer (ALIAS-II) for in situ atmospheric measurements of N2O, CH4, CO, HCL, and NO2 from balloon or remotely piloted aircraft platforms, Applied Optics, 38, 21, 4609-4622, https://doi.org/10.1364/AO.38.004609, 1999.Singer, C. E., Clouser, B. W., Khaykin, S. M., Krämer, M., Cairo, F., Peter, T., Lykov, A., Rolf, C., Spelten, N., Afchine, A., Brunamonti, S., and Moyer, E. J.: Intercomparison of upper tropospheric and lower stratospheric water vapor measurements over the Asian Summer Monsoon during the StratoClim campaign, Atmos. Meas. Tech., 15, 4767–4783, https://doi.org/10.5194/amt-15-4767-2022, 2022.

Sitnikov, N. M., Yushkov, V. A., Afchine, A., Korshunov, L. I., Astakhov, V. I., Ulanovskii, A. E., Kraemer, M., Mangold, A., Schiller, C., and Ravegnani, F.: The FLASH instrument for water vapor measurements on board the high-altitude airplane, Instruments and Experimental Techniques, 50, 113–121, https://doi.org/10.1134/S0020441207010174, 2007.

Solomon, S., Rosenlof, K. H., Portmann, R. W., Daniel, J. S., Davis, S. M., Sanford, T. J., and Plattner, G.-K.: Contributions of stratospheric water vapor to decadal changes in the rate of global warming, Science, 327, 1219–1223, https://doi.org/10.1126/science.1182488, 2010.

Tennyson, J., Bernath, P. F., Campargue, A., Császár, A. G., Daumont, L., Gamache, R. R., Hodges, J. T., Lisak, D., Naumenko, O. V., Rothman, L. S., Tran, H., Zobov, N. F., Buldyreva, J., Boone, C. D., De Vizia, M. D., Gianfrani, L., Hartmann, J.-M., McPheat, R., Weidmann, D., Murray, J., Ngo, N. H., and Polyansky, O. L.: Recommended isolated-line profile for representing high-resolution spectroscopic transitions (IUPAC Technical Report), Pure and Applied Chemistry, 86(12), 1931-1943, https://doi.org/10.1515/pac-2014-0208, 2014.

Tuzson, B., Graf, M., Ravelid, J., Scheidegger, P., Kupferschmid, A., Looser, H., Morales, R. P., and Emmenegger, L.: A compact QCL spectrometer for mobile, high-precision methane sensing aboard drones, Atmos. Meas. Tech., 13, 4715–4726, https://doi.org/10.5194/amt-13-4715-2020, 2020.

UNEP: Montreal Protocol – Kigali Amendment, chap. XXVII, 2. F Amendment to the Montreal Protocol on Substances that Deplete, the Ozone Layer Kigali, Rwanda, 2016.

Vaittinen, O., Metsälä, M., Halonen, L., Persijn, S., Leuenberger, D., and Niederhauser, B.: Effect of moisture on the adsorption of ammonia, Appl. Phys. B 124, 189, https://doi.org/10.1007/s00340-018-7054-2, 2018.

Vömel, H., David, D. E., and Smith, K.: Accuracy of tropospheric and stratospheric water vapor measurements by the cryogenic frost point hygrometer: Instrumental details and observations, J. Geophys. Res.-Atmos., 112, D08305, https://doi.org/10.1029/2006JD007224, 2007.

Vömel, H., Naebert, T., Dirksen, R., and Sommer, M.: An update on the uncertainties of water vapor measurements using cryogenic frost point hygrometers, Atmos. Meas. Tech., 9, 3755–3768, https://doi.org/10.5194/amt-9-3755-2016, 2016.

Werle, P., Mücke, R., and Slemr, F.: The limits of signal averaging in atmospheric trace-gas monitoring by tunable diode-laser absorption spectroscopy (TDLAS), Appl. Phys. B, 57, 131–139, 1993.

Zöger, M., Afchine, A., Eicke, N., Gerhards, M.-T., Klein, E., McKenna, D. S., Mörschel, U., Schmidt, U., Tan, V., Tuitjer, F., Woyke, T., and Schiller, C.: Fast in situ stratospheric hygrometers: A new family of balloon-borne Lyman-α photofragment fluorescence hygrometers, J. Geophys. Res., 104, 1807–1816, 1999.